HHS Public Access

Author manuscript

Front Phys. Author manuscript; available in PMC 2023 July 05.

Published in final edited form as:

Front Phys. 2021 ; 9: . doi:10.3389/fphy.2021.737374.

Multidimensional MRI for Characterization of Subtle Axonal Injury Accelerated Using an Adaptive Nonlocal Multispectral Filter

Dan Benjamini[1,2,3,*], **Mustapha Bouhrara**[4], **Michal E. Komlosh**[1,2,3], **Diego Iacono**[2,3,5,6,7,8,9], **Daniel P. Perl**[2,5,7], **David L. Brody**[2,10], **Peter J. Basser**[1,2]

[1]Section on Quantitative Imaging and Tissue Sciences, National Institute of Child Health and Human Development, National Institutes of Health, Bethesda, MD, United States,

[2]Center for Neuroscience and Regenerative Medicine, Uniformed Services University of the Health Sciences, Bethesda, MD, United States,

[3]The Henry M. Jackson Foundation for the Advancement of Military Medicine (HJF), Bethesda, MD, United States,

[4]Magnetic Resonance Physics of Aging and Dementia Unit, National Institute of Aging, National Institutes of Health, Baltimore, MD, United States,

[5]Brain Tissue Repository and Neuropathology Program, Uniformed Services University (USU), Bethesda, MD, United States,

[6]Department of Neurology, F. Edward Hébert School of Medicine, Uniformed Services University, Bethesda, MD, United States,

[7]Department of Pathology, F. Edward Hébert School of Medicine, Uniformed Services University, Bethesda, MD, United States,

[8]Department of Anatomy, Physiology and Genetics, F. Edward Hébert School of Medicine, Uniformed Services University, Bethesda, MD, United States,

[*]**Correspondence:** Dan Benjamini, dan.benjamini@nih.gov.

AUTHOR CONTRIBUTIONS

DB: conceptualization, design of the study, methodology, software, investigation, data curation, writing—original draft, writing—review and editing, visualization, supervision, and project administration. MB: conceptualization, design of the study, methodology, software, and writing—review and editing. MK: methodology, investigation, and writing—review and editing. DI: methodology, investigation, and writing—review and editing. DP: investigation, methodology, resources, and writing—review and editing. DLB: design of the study, investigation, resources, and writing—review and editing. PB: conceptualization, methodology, resources, writing—review and editing, and funding acquisition. All authors contributed to the article and approved the submitted version.

Conflict of Interest: The authors declare that the research was conducted in the absence of any commercial or financial relationships that could be construed as a potential conflict of interest.

ETHICS STATEMENT

For each case, a next–of-kin or legal representative provided a written consent for donation of the brain for use in research.

SUPPLEMENTARY MATERIAL

The Supplementary Material for this article can be found online at: https://www.frontiersin.org/articles/10.3389/fphy.2021.737374/full#supplementary-material

[9]Neurodegeneration Disorders Clinic, National Institute of Neurological Disorders and Stroke, National Institutes of Health, Bethesda, MD, United States,

[10]Laboratory of Functional and Molecular Imaging, National Institute of Neurological Disorders and Stroke, National Institutes of Health, Bethesda, MD, United States

Abstract

Multidimensional MRI is an emerging approach that simultaneously encodes water relaxation (T_1 and T_2) and mobility (diffusion) and replaces voxel-averaged values with subvoxel distributions of those MR properties. While conventional (i.e., voxel-averaged) MRI methods cannot adequately quantify the microscopic heterogeneity of biological tissue, using subvoxel information allows to selectively map a specific T_1-T_2-diffusion spectral range that corresponds to a group of tissue elements. The major obstacle to the adoption of rich, multidimensional MRI protocols for diagnostic or monitoring purposes is the prolonged scan time. Our main goal in the present study is to evaluate the performance of a nonlocal estimation of multispectral magnitudes (NESMA) filter on reduced datasets to limit the total acquisition time required for reliable multidimensional MRI characterization of the brain. Here we focused and reprocessed results from a recent study that identified potential imaging biomarkers of axonal injury pathology from the joint analysis of multidimensional MRI, in particular voxelwise T_1-T_2 and diffusion-T_2 spectra in human Corpus Callosum, and histopathological data. We tested the performance of NESMA and its effect on the accuracy of the injury biomarker maps, relative to the co-registered histological reference. Noise reduction improved the accuracy of the resulting injury biomarker maps, while permitting data reduction of 35.7 and 59.6% from the full dataset for T_1-T_2 and diffusion-T_2 cases, respectively. As successful clinical proof-of-concept applications of multidimensional MRI are continuously being introduced, reliable and robust noise removal and consequent acquisition acceleration would advance the field towards clinically-feasible diagnostic multidimensional MRI protocols.

Keywords

multidimensional; MRI; diffusion; relaxation; traumatic brain injury; axonal injury; multispectral nonlocal filtering; NESMA

1 INTRODUCTION

Water molecules within biological tissues interact with their local chemical environment via nuclear relaxation processes and follow diffusion patterns trajectories that are governed by the local tissue density and geometry. Using a combination of magnetic field profiles to probe these mechanisms, magnetic resonance (MR) provides exquisite sensitivity to both the chemical composition, through relaxation parameters, and microstructure, through diffusion parameters, of biological tissues.

One fundamental obstacle for using MRI to characterize tissue heterogeneity is the averaging that occurs across the image volume elements, known as voxels (i.e., pixels with thickness). Voxel-averaged images can only provide macroscopic information with respect to the voxel size, which is typically ~1–3 mm^3. In a mammalian brain, an individual voxel contains multiple chemical and physical microenvironments such as axons,

neurons, glia, myelin, and cerebrospinal fluid. Many biological processes-of-interest take place at a microscopic scale that only affects a small portion of any given voxel, which therefore makes them undetectable using conventional voxel-averaged MRI methods. The inability to separate normal and pathological tissue within a voxel is a major contributor to the insensitivity and ensuing non-specificity of conventional MRI methods in detecting abnormal cellular processes.

By simultaneously encoding multiple MR "dimensions", such as relaxation times (T_1 and T_2) [1] and diffusion [2, 3], multidimensional distributions of those MR parameters can provide fingerprints of various chemical and physical microenvironments within the volume-of-interest, which can be traced back to specific materials and cellular components. If combined with imaging [4], multidimensional MRI has the potential to overcome the voxel-averaging limitation by accomplishes two fundamental goals: 1) it provides unique intra-voxel distributions instead of an average over the whole voxel; this allows identification of multiple components within a given voxel [5–7], while 2) the multiplicity of dimensions inherently facilitates their disentanglement; this allows higher accuracy and precision in derived quantitative values [8–11].

Although traditionally multidimensional MR experiments required many repeated acquisitions and therefore have imposed serious time constraints [12], acquisition strategy [13, 14], computational [3, 6, 15, 16], and pulse design [17, 18] technological breakthroughs have significantly reduced the data burden and positioned multidimensional MRI as a powerful emerging imaging modality for studying biological media. Despite of these advances, wide-spread clinical translation still presents challenges, in particular, due to relatively low signal-to-noise ratio (SNR) and the ensuing increased data amount requirement. To address that, we report the use of a nonlocal estimation of multispectral magnitudes (NESMA) filter [19] on multidimensional MRI data to perform noise reduction for reliable parameter determination and further data reduction. To date, NESMA has been successfully used to improve determination of myelin water fraction from multi-spin-echo MR images [20], or cerebral blood flow from arterial spin labeling MR images [21].

We chose to focus and reprocess a subset of data from our recent study that showed multidimensional MRI can uncover subtle axonal injury patterns in the human brain, otherwise inaccessible using conventional quantitative MRI techniques such as diffusion tensor imaging (DTI), T_1 or T_2 maps [22]. The study investigated brain samples derived from human subjects who had sustained traumatic brain injury (TBI) and control brain donors using MRI, followed by co-registered histopathology that included amyloid precursor protein (APP) immunoreactivity to define axonal injury severity [23]. Abnormal multidimensional T_1-T_2, mean diffusivity-T_2 (MD-T_2), and MD-T_1 spectral signatures that were strongly correlated with injured voxels were identified and used to generate axonal injury biomarker maps [22]. Here we study the effect of applying a multispectral nonlocal filter on three representative cases (a control and two TBI cases), with the main goal of evaluating the performance of NESMA on reduced datasets to limit the total acquisition time required for reliable multidimensional MRI characterization of brain tissue. The co-registered APP histology images serve as a "ground truth" reference, thus providing a

unique opportunity to quantitatively evaluate to what extent the accuracy of the injury biomarkers maps is preserved under substantial data reduction.

2 METHODS

2.1 Donors Specimens Employed in the Present Study

We evaluated autopsy-derived brain specimens from two different human brain collections. Formalin-fixed portions of approximately 20 × 20 × 10 mm^3 of the Corpus Callosum (CC) were obtained from one military subject from the DoD/USU Brain Tissue Repository and Neuropathology Program (https://www.researchbraininjury.org, Bethesda, MD; Subject 1), and two civilian subjects enrolled in the Transforming Research and Clinical Knowledge in Traumatic Brain Injury study (TRACK-TBI; https://tracktbi.ucsf.edu/transforming-research-and-clinical-knowledge-tbi) (Subjects 2 and 3). For each case, a next–of-kin or legal representative provided a written consent for donation of the brain for use in research. The brain tissues used have undergone procedures for donation of the tissue, its storage, and use of available clinical information that have been approved by the USU Institutional Review Board (IRB) prior to the initiation of the study. All experiments were performed in accordance with current federal, state, DoD, and NIH guidelines and regulations for postmortem analysis.

Subject 1 was a 44 years old male with no known TBI history and postmortem APP-negative histopathology. Subject 2 was a 60 year old male that died as a result of a intraparenchymal hemorrhage following a motor vehicle accident. Subject 3 was a 49 year old male that died as a result of intraparenchymal and subarachnoid hemorrhages following a fall.

2.2 MRI Acquisition

Prior to MRI scanning, each formalin-fixed brain specimen was transferred to a phosphate-buffered saline (PBS) filled container for 12 days to ensure that any residual fixative was removed from the tissue. The specimen was then placed in a 25 mm tube, and immersed in perfluoropolyether (Fomblin LC/8, Solvay Solexis, Italy), a proton free fluid void of a proton-MRI signal. Specimens were imaged using a 7 T Bruker vertical bore MRI scanner equipped with a microimaging probe and a 25 mm quadrupole RF coil.

Multidimensional data were acquired using a 3D echo planar imaging (EPI) sequence with a total of 56 and 302 images for T_1-T_2 and MD- T_2, respectively, and with 300 μm isotropic spatial resolution, which resulted in respective acquisition times of 4.5 and 17.8 h. To test the feasibility of data reduction using NESMA we derived reduced datasets by sub-sampling the full datasets. The total number of T_1-T_2 images was reduced from 56 to 36 (35.7% decrease), while the total number of MD-T_2 images was reduced from 302 to 122 (59.6% decrease). Further details can be found in the Supplementary Material.

The SNR was always maintained above 100 (defined as the ratio between the average unattenuated signal intensity within a tissue region of interest, and the standard deviation of the signal intensity within the background). The sample temperature was set at 16.8°C.

2.3 Multidimensional MRI Processing

Here we implemented a marginally-constrained, ℓ_2-regularized, nonnegative least square optimization to compute the multidimensional distribution in each voxel, as previously described [8, 24]. It is a well-tested approach that had been proved robust and reliable [2, 14, 25–29], which in this study had resulted in two types of distributions in each voxel: T_1-T_2 and MD-T_2. The 2D T_1-T_2 and MD-T_2 distributions were evaluated on 50 × 50 logarithmically sampled grids using a previously described algorithm [13]. The range for T_1 was 1–10,000 m, the range for T_2 was 1–500 m, and the range for MD was 0.0001–5 μm^2/ms.

If one considers the multidimensional distributions as spectra, it is possible to use them to generate maps of specific spectral components by means of integration over a predefined parameter range generally associated with a spectral peak. The integral value is a number between 0 and 1, representing a certain spectral component (SC) in a given multidimensional distribution, which can be computed in each voxel to generate an image of that specific SC [30]. Here we apply a recently proposed unsupervised algorithm to identify the injury-associated spectral information [22], and generate injury biomarker maps that closely follow APP histopathology.

2.4 The Nonlocal Estimation of Multispectral Magnitudes (NESMA) Filter

For each sample, the multidimensional distributions were derived from the original multidimensional data as well as from data denoised using the NESMA filter to improve accuracy and precision in derived distributions.

We consider K multidimensional images defined on a discrete grid describing the 3D spatial domain spanned by the image. The underlying idea of quantitative filters is to reduce noise by replacing the intensity of a given voxel by an unbiased estimate of its underlying amplitude. This requires selection of voxels that are likely to come from similar tissue. The NESMA filter restores the amplitude, A, of an index voxel, i, based on intensities of M preselected voxels with similar multispectral signal patterns through:

$$A_k(i) = \frac{1}{M}\sum_{j}^{M} S_k(j), \tag{1}$$

where $S_k(j)$ is the measured amplitude in voxel j of frame k. M is the total number of similar voxels defined using the relative Manhattan distance (RMD) between voxel intensities as

$$RMD(i,j) = 100 \times \frac{\sum_{k=1}^{K} |S_k(i) - S_k(j)|}{\sum_{k=1}^{K} S_k(i)}. \tag{2}$$

The RMD was calculated between the index voxel i and all voxels belonging to a relatively large search window of size R, centered around the index voxel i, in which emission and reception B_1 fields and noise standard deviation (SD) were assumed to be approximately constant. The size of the window must be sufficiently large to ensure inclusion of an adequate number of similar voxels, and sufficiently restricted to ensure that the transmission

and reception B_1 fields and noise SD are approximately constant within the window. In this work, we used a relatively conservative window size to avoid introducing bias in the estimated amplitudes. The size of the search window, R, was fixed at 11 × 11 × 11 voxels. Voxels with RMD <5% were considered similar to the index voxel.

2.5 Histopathology

After MRI scanning, each CC tissue block was transferred for histopathological processing. Tissue blocks from each brain specimen were processed using an automated tissue processor (ASP 6025, Leica Biosystems, Nussloch, Germany). After tissue processing, each tissue block was embedded in paraffin and cut in a series of 5 μm-thick consecutive sections on which immunohistochemistry for anti-amyloid precursor protein (APP) was performed (DS9800, Leica Biosystems, Buffalo Grove, IL). Further details can be found in [22].

2.6 Quantification of Axonal Damage

Images of APP stained sections were digitized using an Aperio whole slide scanning scanner system (Leica Biosystems, Richmond, IL) at ×20 magnification. The following steps, all implemented using MATLAB (The Mathworks, Natick, MA), were taken to allow for a quantitative analysis of the APP images. First, the images were transformed into a common, normalized space to enable improved quantitative analysis [31]. Then, the normalized images were deconvolved to unmix the primary (APP) and secondary (hematoxylin and eosin, H&E) stains, and background to three separate channels [32]. Once an APP-only image was obtained, a final thresholding step was taken to exclude non-specific staining and to allow for a subsequent % area calculation.

From each tissue section, based on APP staining, traumatic axonal injury (TAI) lesions were identified by an experienced neuropathologist (DI) as white matter (WM) areas with swollen axonal varicosities, axonal bulbs, or distorted axons. Accordingly, regions of interest (ROI) of normal-appearing WM and TAI lesions were manually defined. Additionally, gray matter (GM) ROIs from adjacent cingulate cortex were defined in all sections. Twelve ROIs, covering together an average 81 mm^2 of tissue, were identified per tissue section. After extracting the ROIs, APP density was expressed as the percentage of total area within the ROI in the binary deconvolved APP image. In total, 36 ROIs from three subjects were included in this study.

3 RESULTS

3.1 Axonal Injury Spectral Signatures Are Preserved After Filtering

We first investigated the spatially-resolved subvoxel T_1-T_2 and MD-T_2 spectral components to assess the effect of NESMA on the derived voxelwise spectra. To do that, it is useful to summarize the 4D information, which consists of 2D images with 50 × 50 spectra in each voxel, as arrays of images with varying subvoxel T_1, T_2, and MD values. To make them more readable, the 50 × 50 spectra were sub-sampled on a 10 × 10 grid. These maps are shown in Figures 1–3 for all three Subjects. Corresponding histological APP images (co-registered with the MRI) are shown on the left panel of Figure 4, with red color indicating abnormal APP accumulation.

Starting with the control case (Subject 1), the spatially-resolved subvoxel T_1-T_2 and MD-T_2 spectral components are shown in Figure 1. The left column shows the results from the unfiltered data (T_1-T_2 and MD-T_2 in Figures 1A, C, respectively), while the right column shows the results from the filtered data (T_1-T_2 and MD-T_2 in Figures 1B, D, respectively). The maps revealed signal components that were spatially consistent with specific tissue types such as white matter and gray matter.

The spatially-resolved subvoxel T_1-T_2 and MD-T_2 spectral components from the first TBI case (Subject 2) are shown in Figure 2. As before, the left column shows the results from the unfiltered data (T_1-T_2 and MD-T_2 in Figures 2A,C, respectively), and the right column shows the results from the filtered data (T_1-T_2 and MD-T_2 in Figures 2B,D, respectively). Similarly to the control case, here too the maps revealed signal components that were spatially consistent with specific tissue types.

The spatially-resolved subvoxel T_1-T_2 and MD-T_2 spectral components from the second TBI case (Subject 3) are shown in Figure 3. Unfiltered (T_1-T_2 and MD-T_2 in Figures 3A, C, respectively) and filtered data (T_1-T_2 and MD-T_2 in Figures 3B, D, respectively) are shown. As before, signal components that were spatially consistent with specific tissue types as a function of T_1, T_2, and MD were revealed.

Figure 4 shows histological images and multidimensional MR-derived injury biomarker maps of the three representative cases. Histological images (red = APP stain) of the control case (Subject 1) show negative APP staining, compared with positive APP staining in the injured samples (Subjects two and 3). We then examine separately the two MRI-derived injury biomarkers, T_1-T_2 and MD-T_2, and show the resulting images obtained using the unfiltered full dataset (as originally published in [22]), the filtered full dataset, and the filtered reduced dataset. In addition, the MRI-derived injury biomarkers obtained by using the unfiltered reduced dataset are shown in Supplementary Figure S1 in the Supplementary Material.

Visual inspection of the different injury biomarker maps shown in Figure 4 and Supplementary Figure S1 revealed that filtering of the data does not result in loss of the spectral information of interest, and furthermore, the filtered images appear qualitatively of higher quality. Importantly, the data reduction in the case of the filtered data did not significantly affect the resulting injury biomarker maps (Figure 4).

3.2 Evaluation of Performance and Correlation With Histology

Evaluation of filtering performance was based upon the extent of noise reduction and feature preservation, and was quantified by computing the structural similarity index (SSIM) values [33] between the injury biomarker maps under the different experimental conditions (e.g., unfiltered, filtered) and the co-registered APP density histological image as reference. All of the SSIM values are shown in Figure 5. In the context of the current study we are most interested in the ability to accelerate the multidimensional MRI acquisition, and therefore the accuracy and quality of the reduced data cases are of particular importance. Compared with the unfiltered and reduced data injury biomarker maps, the SSIM values of the filtered and reduced data images increased by 11.1, 0.9, and 14.3% for the MD-T_2-based biomarker

for Subjects 1 to 3, respectively, and increased by 8.6, 7.7, and 4.6% for the T_1-T_2-based biomarker for Subjects 1 to 3, respectively. All of these increases in SSIM were statistically significant ($p < 0.001$).

To further evaluate the performance of the NESMA filter and the subsequent data reduction, we performed radiological–pathological correlation analyses with histological APP density and all the investigated MRI parameters under the different experimental conditions (e.g., MD-T_2 unfiltered, T_1-T_2 filtered and reduced). Figure 6 summarizes the association between the investigated MR metrics and the pathological findings in normal WM, cortical GM, and TAI ROIs.

To assess the relationship of the MRI parameters with the degree of injury, all tissue ROIs were grouped together and correlated with the APP density (solid lines in Figure 6). All multidimensional injury biomarker cases under every experimental condition were strongly and significantly positively correlated with the APP density (i.e., % area APP). These correlations illustrate how the multidimensional injury biomarker maps provide “true negative”, in the sense that any region outside of the TAI lesions has zero or close to zero intensity.

Of particular interest was the case of the MD-T_2 injury biomarker, where the unfiltered dataset resulted in relatively scattered correlation ($r = 0.565$, $p < 2 \times 10^{-4}$, Figure 6A), which was largely unaffected by the data reduction ($r = 0.557$, $p < 3 \times 10^{-4}$, Figure 6B). Marked improvement was observed after filtering the data, which led to significantly tighter correlation between the MRI biomarker and the histological marker ($r = 0.812$, $p < 2 \times 10^{-9}$, Figure 6C). As can be expected, the 59.6% reduction in the data amount led to some reduction in the radiological–pathological correlation ($r = 0.723$, $p < 4 \times 10^{-7}$, Figure 6D), although still performing better than the unfiltered full MD-T_2 dataset. Furthermore, filtering led to a reduced variance within the ROIs, as seen by the decrease in the 95% confidence intervals (error bars in Figure 6).

The T_1-T_2 injury biomarker derived from the unfiltered dataset had excellent correlation with histological APP density ($r = 0.970$, $p < 1 \times 10^{-22}$, Figure 6E), and therefore, it is not surprising that this strong relationship was maintained under all of the investigated experimental conditions ($r = 0.963$, $p < 1 \times 10^{-20}$, $r = 0.962$, $p < 1 \times 10^{-20}$, and $r = 0.969$, $p < 1 \times 10^{-21}$, Figures 6F–H, for unfiltered and reduced, filtered, and filtered and reduced, respectively).

4 DISCUSSION

Here we report the use of the NESMA filter on multidimensional MRI data, in particular voxelwise T_1-T_2 and MD-T_2 spectra in fixed human Corpus Callosum, to remove noise and reduce total scan time. We focused on results from a recent study that identified potential imaging biomarkers of axonal injury pathology from the joint analysis of multidimensional MRI and histopathological data [22]. These axonal injury maps were shown to be significantly and strongly correlated with histological evidence of axonal injury. Reprocessing these data provided an opportunity to test the performance of the NESMA

filter and its effect on the accuracy of the injury biomarker maps, relative to the histological reference.

Our findings showed that noise reduction in the multidimensional MRI data using an adaptive nonlocal multispectral filter (i.e., NESMA [20]) improved the accuracy of the resulting injury biomarker maps, and furthermore, allowed for data reduction of 35.7 and 59.6% from the full dataset, which led to using only 36 and 122 images in the T_1-T_2 and MD-T_2 cases, respectively.

Specifically, visual inspection and a side-by-side comparison of the unfiltered and filtered subvoxel T_1-T_2 and MD-T_2 spectral components (Figures 1–3) showed that the filtered maps exhibit lower random variations, in particular at the lower ends of the spectra, and that there was no apparent loss of spectral information. For example, Subject 3 exhibited a relatively focal axonal injury at the bottom of the CC (Figure 4, left panel), captured at the lower end of the T_1-T_2 spectra, which was previously associated with axonal injury [22]. Noticeable noise reduction at these spectral lower ends was observed, which is crucial to the robust identification of axonal injury from these multidimensional MRI data.

Visual inspection of the resulting T_1-T_2 and MD-T_2 injury biomarker maps with respect to co-registered APP histological images suggested improved accuracy after applying the NESMA filter, even after the data was reduced (Figure 4). Quantitative evaluation that compared the SSIM between the co-registered APP histological images and injury biomarker maps derived from unfiltered and filtered reduced datasets showed a significant increase as a result of the filtering across all subjects (Figure 5).

We performed radiological–pathological correlation analyses with histological APP density and all the investigated MRI parameters under the different experimental conditions to assess quantitatively whether and to what extent the proposed approach preserves strong correlations even under substantial data reduction (Figure 6). This analysis indicated that not only the correlations were preserved, but furthermore, they were considerably improved, even after data reduction, as a result of filtering the data. Lastly, our results suggest that the previously proposed [22] adaptive method of locating the injury-associated T_1-T_2-MD spectral signature is robust to noise removal procedures and to data reduction.

Common to all *ex vivo* human MRI studies, our data include the effects of post-mortem degeneration, fixation and resulting dehydration. Because T_1, T_2, and diffusion dynamics are different in fixed tissue compared with living systems, further investigation will be needed to establish whether and how the axonal injury-related T_1-T_2-MD range of multidimensional magnetic resonance parameters is altered *in vivo*. In this context it is important to note that our findings are not based on absolute values of T_1, T_2, and MD, which indeed are expected to change *in vivo*. Instead, all of the injury biomarkers maps are generated using the relative signal fraction of an automatically identified T_1-T_2-MD range that does not depend on the actual values of these parameters [22]. We therefore anticipate that *in vivo* spectra will be shifted in all T_1, T_2, and MD dimensions compared to our *ex vivo* findings, however, the distributions of the signal fractions should largely remain similar.

The performance of the NESMA filter does not depend on the particular multidimensional spectra quantification processing pipeline because the filter is applied in the image domain, before its transformed into voxelwise spectra. Here we applied a constrained ℓ_2 regularized inversion framework [13], however, we anticipate that the demonstrated improvement after filtering could be extended to other approaches such as ℓ_1 regularization [34], Monte-Carlo inversion [35, 36], and InSpect [16].

Multidimensional MRI is an emerging approach [37] that is now being applied to address a range of medical conditions such as prediction of pregnancy complications via placenta characterization [9], spinal cord injury [6, 38], prostate cancer [39], breast cancer [40], and axonal injury due to TBI [22]. Recent *in vivo* proof-of-concept applications of subvoxel T_1-T_2 correlation spectra using 105 images [41] and of subvoxel diffusion-T_1 correlation spectra using 363 [11] and 304 [42] images are promising. Here we showed that accurate and robust subvoxel T_1-T_2 and MD-T_2 correlation spectra can be obtained using only 36 and 122 images, respectively, by using a constrained optimization data processing framework (i.e., MADCO [13]) in conjunction with applying the NESMA filter to reduce noise. A reliable and robust noise removal and consequent acquisition acceleration should further advance the field towards clinically-feasible diagnostic multidimensional MRI protocols.

Supplementary Material

Refer to Web version on PubMed Central for supplementary material.

ACKNOWLEDGMENTS

We thank the subjects' families that consented for brain donations for the better understanding of TBI consequences. The authors thank Patricia Lee, Nichelle Gray and Paul Gegbeh for their valuable technical work. We are grateful to Stacey Gentile, Deona Cooper and Harold Kramer Anderson for their administrative assistance. We thank the TRACK-TBI Investigators (https://tracktbi.ucsf.edu/transforming-research-and-clinical-knowledge-tbi). The opinions expressed herein are those of the authors and are not necessarily representative of those of the Uniformed Services University of the Health Sciences (USUHS), the Department of Defense (DOD), the NIH or any other US government agency.

FUNDING

This research was partially supported by a grant from the U.S. Department of Defense, Program Project 308430 Uniformed Services University of the Health Sciences (USUHS). Support for this work also included funding from the U.S. Department of Defense to the Brain Tissue Repository and Neuropathology Program, Center for Neuroscience and Regenerative Medicine (CNRM). DB and MEK were supported by the CNRM Neuroradiology-Neuropathology Correlations Core. MB was supported by the Intramural Research Program of the National Institute on Aging. DI, DPP, and DLB were supported by the CNRM and USUHS. PJB was supported by the Intramural Research Program of the Eunice Kennedy Shriver National Institute of Child Health and Human Development.

DATA AVAILABILITY STATEMENT

The datasets generated and analyzed during the current study are available from the corresponding author on reasonable request. Requests to access these datasets should be directed to andlt; basserp@mail.nih.gov.

REFERENCES

1. English AE, Whittall KP, Joy MLG, and Henkelman RM. Quantitative Two-Dimensional Time Correlation Relaxometry. Magn Reson Med (1991) 22: 425–34. doi:10.1002/mrm.1910220250 [PubMed: 1812377]
2. Hürlimann MD, Flaum M, Venkataramanan L, Flaum C, Freedman R, and Hirasaki GJ. Diffusion-relaxation Distribution Functions of Sedimentary Rocks in Different Saturation States. Magn Reson Imaging (2003) 21: 305–10. doi:10.1016/s0730-725x(03)00159-0 [PubMed: 12850723]
3. Topgaard D Multidimensional Diffusion MRI. J Magn Reson (2017) 275: 98–113. doi:10.1016/j.jmr.2016.12.007 [PubMed: 28040623]
4. Benjamini D, and Basser PJ. Multidimensional Correlation MRI. NMR Biomed (2020) 33:e4226. doi:10.1002/nbm.4226 [PubMed: 31909516]
5. de Almeida Martins JP, and Topgaard D. Two-Dimensional Correlation of Isotropic and Directional Diffusion Using NMR. Phys Rev Lett (2016) 116: 087601. doi:10.1103/PhysRevLett.116.087601 [PubMed: 26967442]
6. Kim D, Doyle EK, Wisnowski JL, Kim JH, and Haldar JP. Diffusion-relaxation Correlation Spectroscopic Imaging: A Multidimensional Approach for Probing Microstructure. Magn Reson Med (2017) 78:2236–49. doi:10.1002/mrm.26629 [PubMed: 28317261]
7. Benjamini D, and Basser PJ. Water Mobility Spectral Imaging of the Spinal Cord: Parametrization of Model-free Laplace MRI. Magn Reson Imaging (2019) 56:187–93. doi:10.1016/j.mri.2018.12.001 [PubMed: 30584915]
8. Benjamini D, and Basser PJ. Magnetic Resonance Microdynamic Imaging Reveals Distinct Tissue Microenvironments. NeuroImage (2017) 163:183–96. doi:10.1016/j.neuroimage.2017.09.033 [PubMed: 28943412]
9. Slator PJ, Hutter J, Palombo M, Jackson LH, Ho A, Panagiotaki E, et al. Combined Diffusion-relaxometry MRI to Identify Dysfunction in the Human Placenta. Magn Reson Med (2019) 82:95–106. doi:10.1002/mrm.27733 [PubMed: 30883915]
10. de Almeida Martins JP, Tax CMW, Reymbaut A, Szczepankiewicz F, Chamberland M, Jones DK, et al. Computing and Visualising Intra-voxel Orientation-specific Relaxation-Diffusion Features in the Human Brain. Hum Brain Mapp (2021) 42:310–28. doi:10.1002/hbm.25224 [PubMed: 33022844]
11. Reymbaut A, Critchley J, Durighel G, Sprenger T, Sughrue M, Bryskhe K, et al. Toward Nonparametric Diffusion- Characterization of Crossing Fibers in the Human Brain. Magn Reson Med (2021) 85:2815–27. doi:10.1002/mrm.28604 [PubMed: 33301195]
12. Benjamini D Chapter 10. Nonparametric Inversion of Relaxation and Diffusion Correlation Data. In: Topgaard D, editor. Advanced Diffusion Encoding Methods in MRI. Cambridge, UK: Royal Society of Chemistry (2020). p. 278–316. chap. 10. doi:10.1039/9781788019910-00278
13. Benjamini D, and Basser PJ. Use of Marginal Distributions Constrained Optimization (MADCO) for Accelerated 2D MRI Relaxometry and Diffusometry. J Magn Reson (2016) 271:40–5. doi:10.1016/j.jmr.2016.08.004 [PubMed: 27543810]
14. Benjamini D, and Basser PJ. Towards Clinically Feasible Relaxation-Diffusion Correlation MRI Using MADCO. Microporous Mesoporous Mater (2018) 269: 93–6. doi:10.1016/j.micromeso.2017.02.001 [PubMed: 30220874]
15. Bai R, Cloninger A, Czaja W, and Basser PJ. Efficient 2D MRI Relaxometry Using Compressed Sensing. J Magn Reson (2015) 255:88–99. doi:10.1016/j.jmr.2015.04.002 [PubMed: 25917134]
16. Slator PJ, Hutter J, Marinescu RV, Palombo M, Jackson LH, Ho A, et al. Data-Driven Multi-Contrast Spectral Microstructure Imaging with InSpect: INtegrated SPECTral Component Estimation and Mapping. Med Image Anal (2021) 71:102045. doi:10.1016/j.media.2021.102045 [PubMed: 33934005]
17. Hutter J, Slator PJ, Christiaens D, Teixeira RPAG, Roberts T, Jackson L, et al. Integrated and Efficient Diffusion-Relaxometry Using ZEBRA. Sci Rep (2018) 8:15138. doi:10.1038/s41598-018-33463-2 [PubMed: 30310108]
18. Manhard MK, Stockmann J, Liao C, Park D, Han S, Fair M, et al. A Multi-inversion Multi-echo Spin and Gradient echo echo Planar Imaging Sequence with Low Image Distortion for Rapid

Quantitative Parameter Mapping and Synthetic Image Contrasts. Magn Reson Med (2021) 86:866–80. doi:10.1002/mrm.28761 [PubMed: 33764563]

19. Bouhrara M, Bonny J-M, Ashinsky BG, Maring MC, and Spencer RG. Noise Estimation and Reduction in Magnetic Resonance Imaging Using a New Multispectral Nonlocal Maximum-Likelihood Filter. IEEE Trans Med Imaging (2017) 36:181–93. doi:10.1109/tmi.2016.2601243 [PubMed: 27552743]
20. Bouhrara M, Reiter DA, Maring MC, Bonny J-M, and Spencer RG. Use of the NESMA Filter to Improve Myelin Water Fraction Mapping with Brain MRI. J Neuroimaging (2018) 28:640–9. doi:10.1111/jon.12537 [PubMed: 29999204]
21. Bouhrara M, Lee DY, Rejimon AC, Bergeron CM, and Spencer RG. Spatially Adaptive Unsupervised Multispectral Nonlocal Filtering for Improved Cerebral Blood Flow Mapping Using Arterial Spin Labeling Magnetic Resonance Imaging. J Neurosci Methods (2018) 309:121–31. doi:10.1016/j.jneumeth.2018.08.018 [PubMed: 30130609]
22. Benjamini D, Iacono D, Komlosh ME, Perl DP, Brody DL, and Basser PJ. Diffuse Axonal Injury Has a Characteristic Multidimensional MRI Signature in the Human Brain. Brain (2021) 144:800–16. doi:10.1093/brain/awaa447 [PubMed: 33739417]
23. Johnson VE, Stewart W, and Smith DH. Axonal Pathology in Traumatic Brain Injury. Exp Neurol (2013) 246:35–43. doi:10.1016/j.expneurol.2012.01.013 [PubMed: 22285252]
24. Pas K, Komlosh ME, Perl DP, Basser PJ, and Benjamini D. Retaining Information from Multidimensional Correlation MRI Using a Spectral Regions of Interest Generator. Sci Rep (2020) 10:3246. doi:10.1038/s41598-020-60092-5 [PubMed: 32094400]
25. Provencher SW. A Constrained Regularization Method for Inverting Data Represented by Linear Algebraic or Integral Equations. Comp Phys Commun (1982) 27:213–27. doi:10.1016/0010-4655(82)90173-4
26. Kroeker RM, and Henkelman MR. Analysis of Biological NMR Relaxation Data with Continuous Distributions of Relaxation Times. J Magn Reson (1969) 69:218–35. doi:10.1016/0022-2364(86)90074-0
27. Song Y-Q, Venkataramanan L, Hürlimann MD, Flaum M, Frulla P, and Straley C. T1-T2 Correlation Spectra Obtained Using a Fast Two-Dimensional Laplace Inversion. J Magn Reson (2002) 154:261–8. doi:10.1006/jmre.2001.2474 [PubMed: 11846583]
28. Mitchell J, Chandrasekera TC, and Gladden LF. Numerical Estimation of Relaxation and Diffusion Distributions in Two Dimensions. Prog Nucl Magn Reson Spectrosc (2012) 62:34–50. doi:10.1016/j.pnmrs.2011.07.002 [PubMed: 22364615]
29. Celik H, Bouhrara M, Reiter DA, Fishbein KW, and Spencer RG. Stabilization of the Inverse Laplace Transform of Multiexponential Decay through Introduction of a Second Dimension. J Magn Reson (2013) 236:134–9. doi:10.1016/j.jmr.2013.07.008 [PubMed: 24035004]
30. Labadie C, Lee JH, Vetek G, and Springer CS. Relaxographic Imaging. J Magn Reson Ser B (1994) 105:99–112. doi:10.1006/jmrb.1994.1109 [PubMed: 7952937]
31. Macenko M, Niethammer M, Marron JS, Borland D, and Xiaojun Guan JT. A Method for Normalizing Histology Slides for Quantitative Analysis. In IEEE International Symposium on Biomedical Imaging. From Nano to MacroIEEE (2009) p. 1107–10. doi:10.1109/ISBI.2009.5193250
32. Ruifrok AC, and Johnston DA. Quantification of Histochemical Staining by Color Deconvolution. Anal Quant Cytol Histol (2001) 23:291–9. [PubMed: 11531144]
33. Wang Z, Bovik AC, Sheikh HR, and Simoncelli EP. Image Quality Assessment: From Error Visibility to Structural Similarity. IEEE Trans Image Process (2004) 13:600–12. doi:10.1109/tip.2003.819861 [PubMed: 15376593]
34. Reci A, Sederman AJ, and Gladden LF. Obtaining Sparse Distributions in 2D Inverse Problems. J Magn Reson (2017) 281:188–98. doi:10.1016/j.jmr.2017.05.010 [PubMed: 28623744]
35. Prange M, and Song Y-Q. Quantifying Uncertainty in NMR Spectra Using Monte Carlo Inversion. J Magn Reson (2009) 196:54–60. doi:10.1016/j.jmr.2008.10.008 [PubMed: 18952474]
36. de Almeida Martins JP, and Topgaard D. Multidimensional Correlation of Nuclear Relaxation Rates and Diffusion Tensors for Model-free Investigations of Heterogeneous Anisotropic Porous Materials. Sci Rep (2018) 8:2488. doi:10.1038/s41598-018-19826-9 [PubMed: 29410433]

37. Slator PJ, Palombo M, Miller KL, Westin C, Laun F, Kim D, et al. Combined Diffusion-Relaxometry Microstructure Imaging: Current Status and Future Prospects. Magn Reson Med (2021). doi:10.1002/mrm.28963

38. Benjamini D, Hutchinson EB, Komlosh ME, Comrie CJ, Schwerin SC, Zhang G, et al. Direct and Specific Assessment of Axonal Injury and Spinal Cord Microenvironments Using Diffusion Correlation Imaging. NeuroImage (2020) 221:117195. doi:10.1016/j.neuroimage.2020.117195 [PubMed: 32726643]

39. Zhang Z, Wu HH, Priester A, Magyar C, Afshari Mirak S, Shakeri S, et al. Prostate Microstructure in Prostate Cancer Using 3-T MRI with Diffusion-Relaxation Correlation Spectrum Imaging: Validation with Whole-Mount Digital Histopathology. Radiology (2020) 296:348–55. doi:10.1148/radiol.2020192330 [PubMed: 32515678]

40. Naranjo ID, Reymbaut A, Brynolfsson P, Lo Gullo R, Bryskhe K, Topgaard D, et al. Multidimensional Diffusion Magnetic Resonance Imaging for Characterization of Tissue Microstructure in Breast Cancer Patients: A Prospective Pilot Study. Cancers (2021) 13:1606. doi:10.3390/cancers13071606 [PubMed: 33807205]

41. Kim D, Wisnowski JL, Nguyen CT, and Haldar JP. Multidimensional Correlation Spectroscopic Imaging of Exponential Decays: From Theoretical Principles to *In Vivo* Human Applications. NMR Biomed (2020) 33. doi:10.1002/nbm.4244

42. Avram AV, Sarlls JE, and Basser PJ. Whole-Brain Imaging of Subvoxel T1-Diffusion Correlation Spectra in Human Subjects. Front Neurosci (2021) 15: 671465. doi:10.3389/fnins.2021.671465 [PubMed: 34177451]

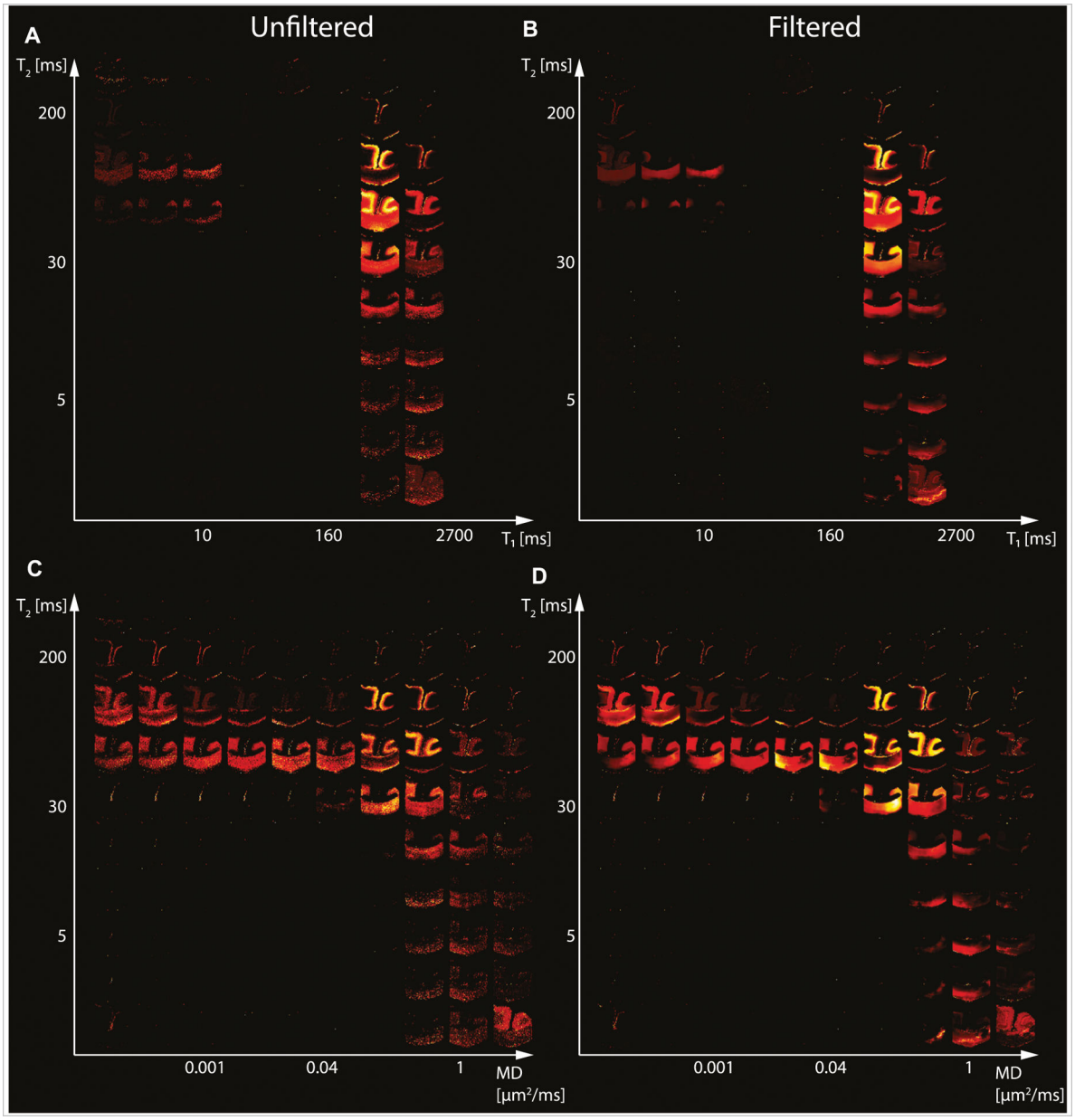

FIGURE 1 |.

Maps of 2D probability density functions (i.e., 2D normalized spectra) from Subject 1 (control) of **(A)** unfiltered and **(B)** filtered subvoxel T_1-T_2 values reconstructed on a 10 × 10 grid of subvoxel T_1 values (horizontal axes) and subvoxel T_2 values (vertical axes), and maps of **(C)** unfiltered and **(D)** filtered subvoxel MD-T_2 values reconstructed on a 10 × 10 grid of subvoxel MD values (horizontal axes) and subvoxel T_2 values (vertical axes).

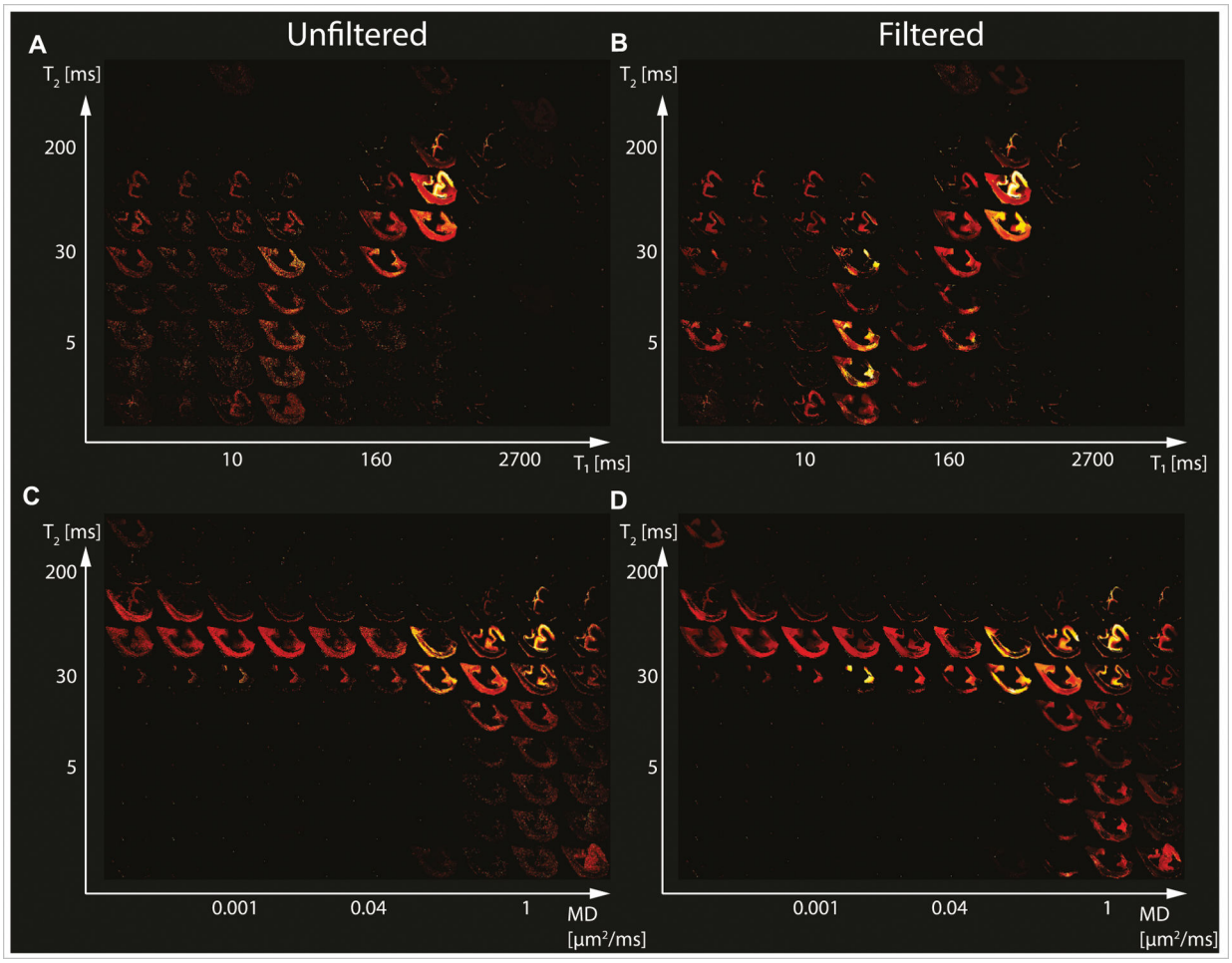

FIGURE 2 |.

Maps of 2D probability density functions (i.e., 2D normalized spectra) from Subject 2 (TBI) of **(A)** unfiltered and **(B)** filtered subvoxel T_1-T_2 values reconstructed on a 10 × 10 grid of subvoxel T_1 values (horizontal axes) and subvoxel T_2 values (vertical axes), and maps of **(C)** unfiltered and **(D)** filtered subvoxel MD-T_2 values reconstructed on a 10 × 10 grid of subvoxel MD values (horizontal axes) and subvoxel T_2 values (vertical axes).

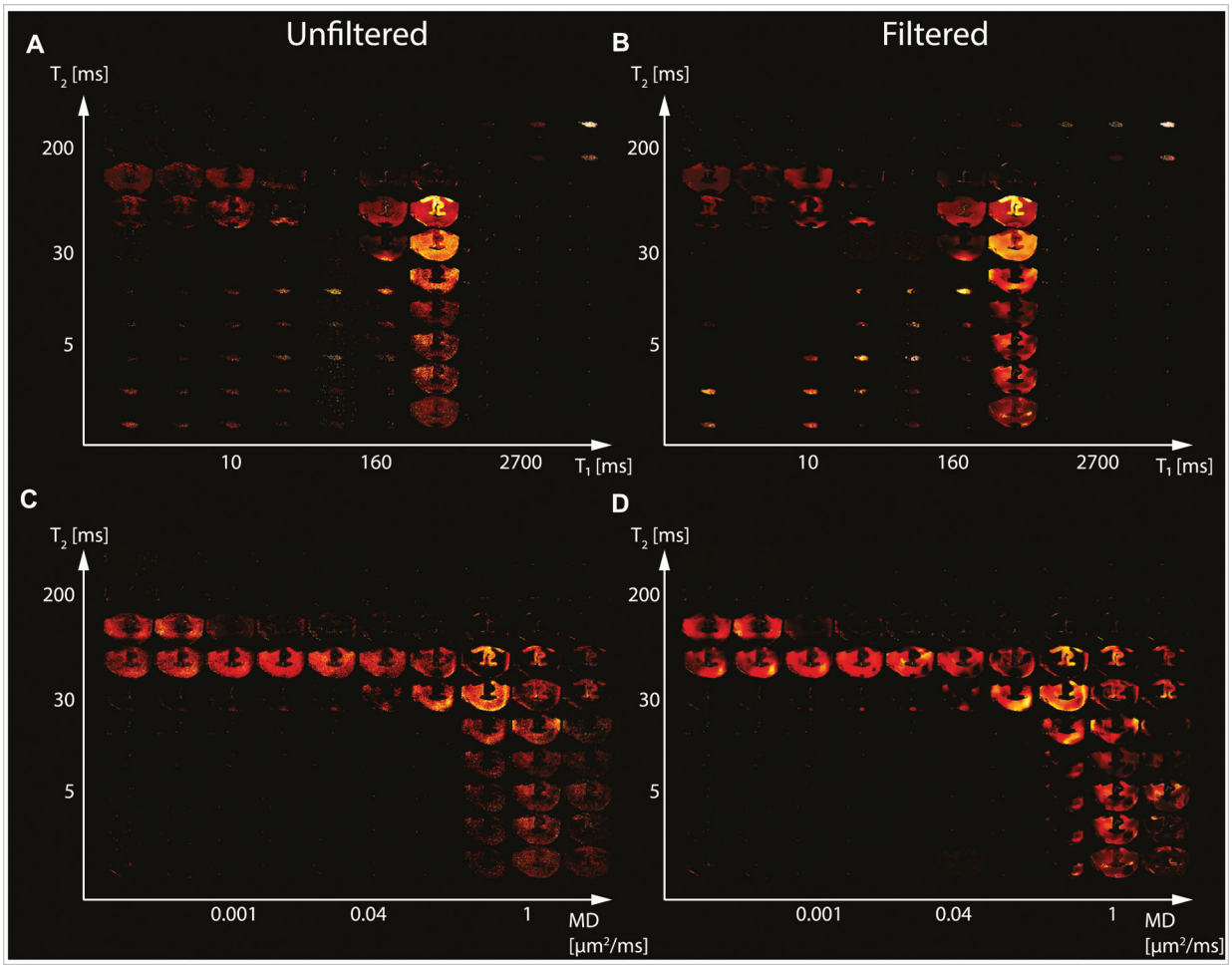

FIGURE 3 |.

Maps of 2D probability density functions (i.e., 2D normalized spectra) from Subject 3 (TBI) of **(A)** unfiltered and **(B)** filtered subvoxel T_1-T_2 values reconstructed on a 10 × 10 grid of subvoxel T_1 values (horizontal axes) and subvoxel T_2 values (vertical axes), and maps of **(C)** unfiltered and **(D)** filtered subvoxel MD-T_2 values reconstructed on a 10 × 10 grid of subvoxel MD values (horizontal axes) and subvoxel T_2 values (vertical axes).

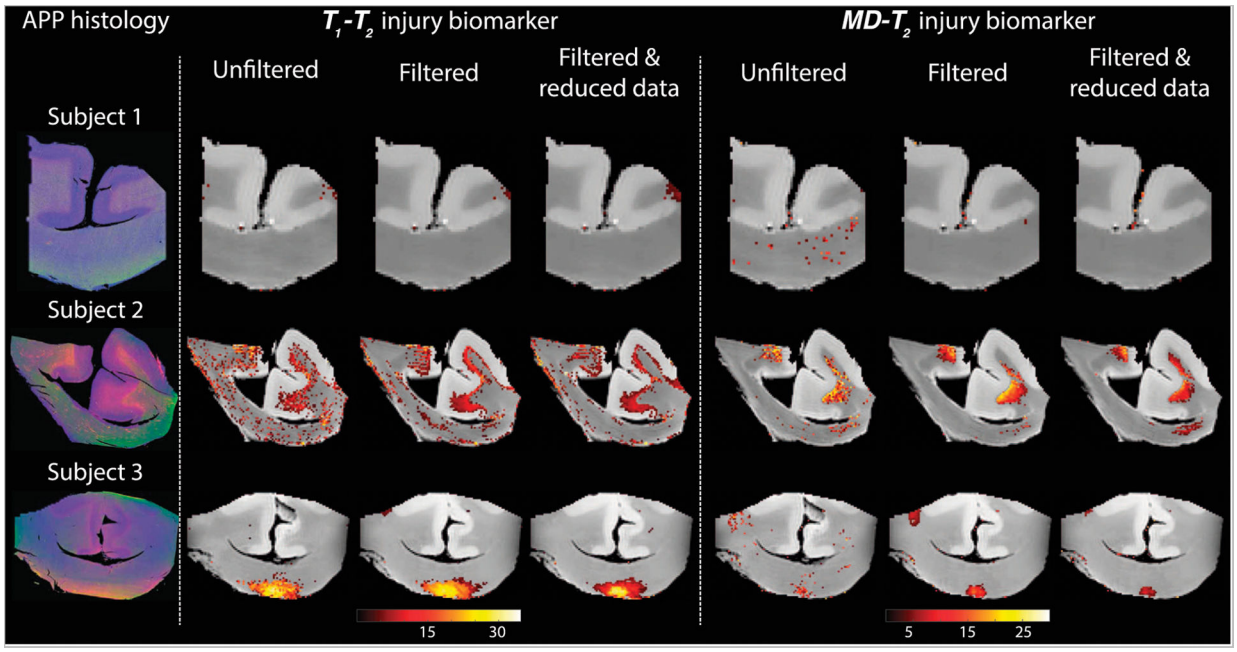

FIGURE 4 |.

Histological images and multidimensional MR-derived injury biomarker maps of three representative cases, and under different conditions (**left to right:** unfiltered, filtered, and filtered and reduced data). Deconvolved histological APP images (co-registered with the MRI) are shown on the left panel, red = APP stain (**top to bottom:** control, and two TBI cases). All multidimensional injury maps were thresholded at 10% of the maximal intensity and overlaid on grayscale proton density images. Multidimensional injury maps of Subject 1 (control) show absent of significant injury under all experimental conditions. Multidimensional injury maps of Subject 2 (TBI) show substantial injury along the white-gray matter interface under all experimental conditions. Multidimensional injury maps of Subject 3 (TBI) show substantial injury at the bottom of the CC under all experimental conditions.

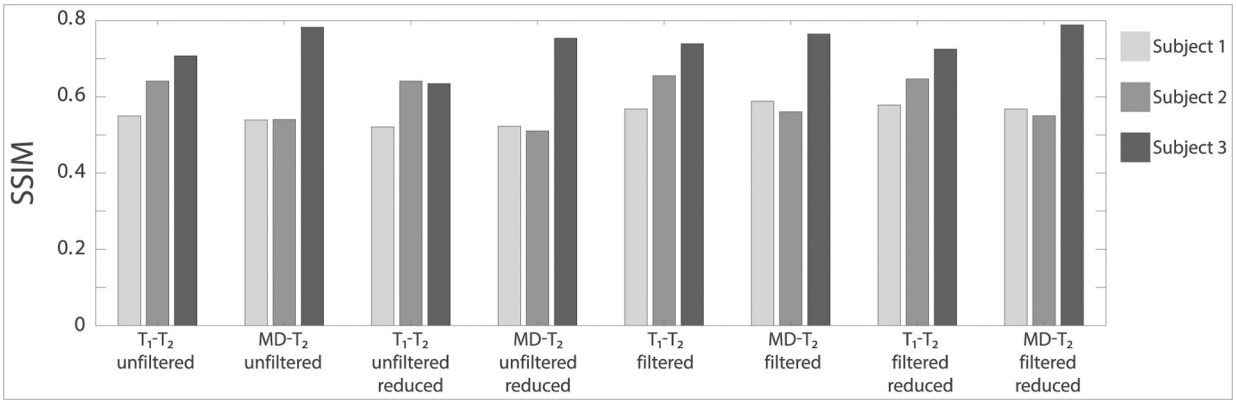

FIGURE 5 |.

The structural similarity index (SSIM) values between the injury biomarker images under the different experimental conditions (e.g., T_1-T_2 unfiltered, MD-T_2 filtered reduced data) and the co-registered APP density histological image as reference. The three bars at each condition represent the different Subjects (blue = Subject 1, red = Subject 2, and yellow = Subject 3).

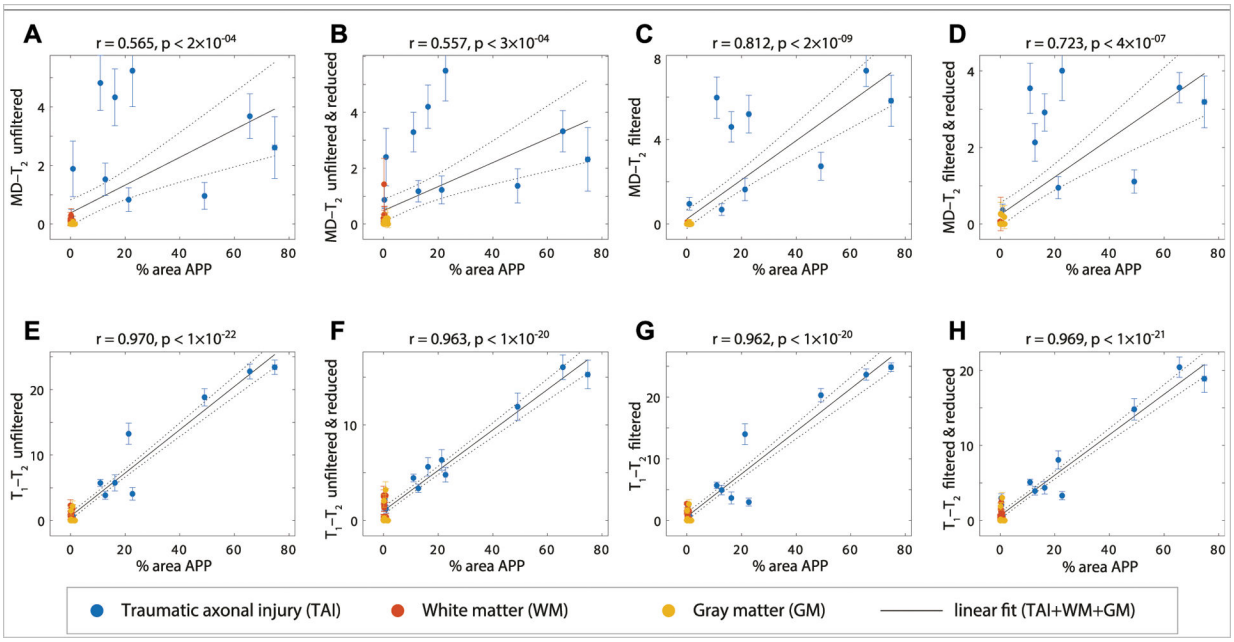

FIGURE 6 |.

APP density (% area) from 36 tissue regions (APP-positive regions from each TBI case, WM and GM regions), and its correlation with injury biomarker parameter under different experimental conditions. Individual data points represent the mean ROI value from each post-mortem tissue sample. Scatterplots of the mean (with 95% confidence interval error bars) % area APP and **(A)** MD-T_2 unfiltered **(B)** MD-T_2 unfiltered and reduced **(C)** MD-T_2 filtered **(D)** MD-T_2 filtered and reduced **(E)** T_1-T_2 unfiltered **(F)** T_1-T_2 unfiltered and reduced **(G)** T_1-T_2 filtered, and **(H)** T_1-T_2 filtered and reduced, show positive and significant correlation with APP density.